



Cite this: *Environ. Sci.: Water Res. Technol.*, 2025, 11, 1951

Oxygen vacancy-engineered $\text{Bi}_2\text{O}_2\text{CO}_3$ nanosheets for enhanced photodegradation of pharmaceuticals and personal care products in water†

Helena Pérez del Pulgar, ^a Josefa Ortiz-Bustos, ^a Santiago Gómez-Ruiz, ^{ab} Isabel del Hierro *^{ab} and Yolanda Pérez *^{ac}

Defect engineering has emerged as a versatile approach for tailoring the properties of materials to meet specific functional applications and improve their properties. In the context of environmental remediation, the introduction of surface oxygen vacancies in semiconductor materials has demonstrated to be a highly effective strategy to enhance molecular adsorption and contaminants' degradation. Herein, we reported the synthesis of $\text{Bi}_2\text{O}_2\text{CO}_3$ nanosheets with surface oxygen vacancies (OVs) via the controlled addition of an accessible, non-toxic and versatile ionic liquid, choline hydroxide. The presence of OVs was confirmed by X-ray photoelectron spectroscopy (XPS) and electrochemical techniques, including cyclic voltammetry (CV) and differential pulse voltammetry (DPV). Upon optimizing the concentration of choline hydroxide, it was found that the addition of 10% of choline hydroxide yielded a material, Chol10%- $\text{Bi}_2\text{O}_2\text{CO}_3$, with significantly enhanced adsorptive and photocatalytic performance. This material efficiently removed not only antibiotics such as ciprofloxacin (97.5% in 20 min) and sulfamethoxazole (98.5% in 60 min), but also a UV filter compound, benzophenone-4 (92.4% in 180 min), which are representative of pharmaceuticals and personal care products (PPCPs) of high environmental concern. Mechanistic studies into reactive oxygen species involved in the photocatalytic process, together with a thorough study of the energy band structure, revealed that Chol10%- $\text{Bi}_2\text{O}_2\text{CO}_3$ generates both hydroxyl (OH^\cdot) and superoxide (O_2^\cdot) radicals, which are essential for the efficient degradation of the recalcitrant UV filter compound, showing the potential of oxygen vacancy-engineered $\text{Bi}_2\text{O}_2\text{CO}_3$ nanosheets as promising platforms for water purification and environmental remediation applications.

Received 20th April 2025,
Accepted 15th June 2025

DOI: 10.1039/d5ew00367a

rsc.li/es-water



Water impact

A highly effective Chol10%- $\text{Bi}_2\text{O}_2\text{CO}_3$ photocatalyst with surface oxygen vacancies was developed, capable of removing various pharmaceuticals and personal care products (PPCPs) of significant environmental concern from water. These include antibiotics such as ciprofloxacin (97.5% removal in 20 min) and sulfamethoxazole (98.5% in 60 min), as well as a UV filter compound, benzophenone-4 (92.4% in 180 min).

1. Introduction

The presence of pharmaceuticals and personal care products (PPCPs) in aquatic environments has become a significant

global issue due to their detrimental impact on the health of both aquatic organisms and humans.¹ Among PPCPs, antibiotics like ciprofloxacin (CIP) and sulfamethoxazole (SMZ) have been detected in various water sources at high concentrations, which are known to promote the emergence of antibiotic-resistant bacteria² and the inhibition of algae growth, affecting photosynthesis in aquatic environments.³ For instance, CIP concentrations as high as 6.5 mg L^{-1} have been reported in waters near pharmaceutical factories,⁴ while SMZ concentrations have ranged from 0.1 to $32 \text{ }\mu\text{g L}^{-1}$ in drinking water.⁵

In addition to antibiotics, UV filters, widely used as sun-blocking agents in personal care products (e.g. sunscreens,

^a COMET-NANO Group, Departamento de Biología y Geología, Física y Química Inorgánica, ESCET, Universidad Rey Juan Carlos, C/Tulipán s/n, 28933 Móstoles, Madrid, Spain. E-mail: isabel.hierro@urjc.es, yolanda.cortes@urjc.es

^b Instituto de Investigación de Tecnologías para la Sostenibilidad, Universidad Rey Juan Carlos, Spain

^c Advanced Porous Materials Unit, IMDEA Energy, Av. Ramón de la Sagra 3, 28935 Móstoles, Madrid, Spain

† Electronic supplementary information (ESI) available. See DOI: <https://doi.org/10.1039/d5ew00367a>

shampoos) and industrial applications (e.g., food packaging, paints)⁶ are of growing concern for the scientific community. The most common UV filter compound, namely, benzophenone-4 (BP-4), is particularly resistant to degradation and has been detected at concerning concentrations (ranging from 0.2 to 5.8 $\mu\text{g L}^{-1}$ in influents and 0.1 to 4.3 $\mu\text{g L}^{-1}$ in effluents of wastewater treatment plants and from 0.003 to 1.3 $\mu\text{g L}^{-1}$ in surface waters).⁷ BP-4's ecotoxicological impact, along with its endocrine-disrupting potential induces significant risks to aquatic organisms.⁸ Due to these risks, the development of cost-efficient methods to eliminate PPCPs from water is urgently needed.

In this context, the removal of BP-4 still remains a challenge.^{9,10} Advanced oxidation processes (AOPs) have been explored for the degradation of BP-4, but complete elimination occasionally requires the use of chemical oxidants such as peroxyomonosulfate¹¹ and/or hydrogen peroxide.¹² Other methods, including UV/chlorine disinfection,¹³ anaerobic biodegradation⁷ and adsorption¹⁴ face some limitations, such as the formation of toxic by-products or high regeneration costs for adsorbents. Therefore, the development of more efficient and environmentally friendly methods for BP-4 is imperative. In this sense, photocatalysis is a promising process, as irradiation of a semiconductor with light of suitable energy excites electrons from the valence band (VB) to the conduction band (CB), leaving behind holes (h^+) in the VB. These charge carriers facilitate the formation of reactive oxygen species, such as superoxide (O_2^-) and hydroxyl radicals ($\cdot\text{OH}$), which can subsequently degrade contaminants.^{15,16}

$\text{Bi}_2\text{O}_2\text{CO}_3$, a low-cost, non-toxic, robust and highly active photocatalyst, has demonstrated high potential for removing water contaminants. However, its performance is limited, because of its limited adsorption capacity, and insufficient presence of oxygen vacancies, among other drawbacks. To overcome these limitations, it is necessary to modify it to intrinsically enhance its photocatalytic and adsorption performance. Some strategies that have been used more efficiently include ion doping,¹⁷ surface¹⁸ and/or morphology modification¹⁹ and creating defects (e.g., OVs).²⁰ For instance, Guo *et al.*²¹ reported $\text{Bi}_2\text{O}_2\text{CO}_3$ nanosheets with functional groups and OVs, which were synthesized using a hydrothermal method with ammonia solution and ethylene glycol as a solvent mixture. Feng *et al.*²² prepared $\text{Bi}_2\text{O}_2\text{CO}_3$ materials enriched with surface OVs by using different amounts of glyoxal at room temperature, enhancing their active sites. Similarly, Lu *et al.*²³ improved the photocatalytic properties of $\text{Bi}_2\text{O}_2\text{CO}_3$ systems *via* a heat-treatment method (350 °C for 2 h), resulting in OV-induced $\text{Bi}_2\text{O}_3/\text{Bi}_2\text{O}_2\text{CO}_3$ materials. Thus, these findings support that surface OV modification is a viable approach for enhancing the photocatalytic and adsorption properties of $\text{Bi}_2\text{O}_2\text{CO}_3$.

On the other hand, choline based ionic liquids have attracted considerable attention due to their low-toxicity, biocompatibility and biodegradability. The choline cation

($[\text{Chol}]^+$), a component of vitamin B₄, is classified as safe by various food regulatory agencies such as the U.S. Food and Drug Administration and the European Food Safety Agency.²⁴ In particular, choline hydroxide, as a readily available ionic liquid, has been widely used in various chemical reactions including base-catalyzed, ring opening, Knoevenagel–Michael and aldol reactions.²⁵

Inspired by these findings, we propose an alternative strategy to enhance both the photocatalytic and adsorption performance of $\text{Bi}_2\text{O}_2\text{CO}_3$ *via* surface modification with choline hydroxide (CholOH). This approach promotes synergistic effects, including an increase of specific surface area and the generation of OVs. The resulting $\text{Bi}_2\text{O}_2\text{CO}_3$ -based materials were characterized by using a wide variety of techniques including spectroscopy (FTIR, NMR, XPS, UV-vis and PL) and microscopy (TEM and FESEM), as well as textural and (photo)electrochemical methods (CV, DPV, EIS and photocurrent analysis) to investigate the properties of the modified systems prepared with varying amounts of choline hydroxide. Notably, our studies show that using an optimized amount of ionic liquid enhances the performance of $\text{Bi}_2\text{O}_2\text{CO}_3$ systems, improving both the adsorption and degradation of the studied antibiotics (CIP and SMZ) and the UV filter BP-4 (Table S1†). This resulted in high total organic carbon (TOC) removals (>80% mineralization for CIP and >75% mineralization for SMZ and BP-4). Trapping experiments, identification of degradation compounds, Mott–Schottky analysis and band structure calculations revealed several insights on the mechanism and energy band alignment, highlighting the role of ROS in pollutant removal. Thus, the approach presented here provides with a simple solution for the preparation of high-performance systems, by a choline-modification of $\text{Bi}_2\text{O}_2\text{CO}_3$ as an environmentally friendly alternative for the remediation of emerging water pollutants.

2. Experimental section

2.1. Materials

Bismuth(III) nitrate pentahydrate $\geq 98\%$ ($\text{Bi}(\text{NO}_3)_3 \cdot 5\text{H}_2\text{O}$) was acquired from Chem Lab and sodium carbonate (Na_2CO_3 , anhydrous) from Scharlau. Choline hydroxide (CholOH, 45 wt% in water) and ciprofloxacin 98% (CIP) were purchased from Acros Organics. Sulfamethoxazole (SMZ) and benzophenone-4 (BP-4) were acquired from Fluorochem and Aldrich-Merck, respectively. Acetic acid and ethanol were purchased from Carlo ERBA Reagents and VWR Chemical, respectively. Water was filtered using a Millipore Milli-Q system (Waters, USA).

2.2. Synthesis of $\text{Bi}_2\text{O}_2\text{CO}_3$ -based materials

$\text{Bi}_2\text{O}_2\text{CO}_3$ was prepared according to a previously reported method with some modifications.²⁶ In a typical synthesis, 1.94 g (4 mmol) of $\text{Bi}(\text{NO}_3)_3 \cdot 5\text{H}_2\text{O}$ was dissolved in 6 mL of acetic acid and the mixture was stirred for 1 h (solution A). Then, 6.36 g of Na_2CO_3 (60 mmol) was dissolved in Milli-Q



water and CholOH (5, 10, or 20% wt) was added to give solution B. Subsequently, solution B was added dropwise to solution A and the mixture was then stirred for 1 h. The resulting solid was filtered, washed with water and ethanol, and dried overnight at 70 °C. Subsequently, the solid was calcined at 260 °C for 4 h. The samples were denoted as CholX%-Bi₂O₂CO₃ (X = 5, 10, and 20). For comparison purposes Bi₂O₂CO₃ was also prepared using the same method but without adding the ionic liquid.

2.3. Characterization

Powder X-ray diffraction (PXRD) patterns were acquired using a Phillips diffractometer model PW3040/00 X'Pert MPD/MRD at 45 kV and 40 mA, with Cu-K α radiation ($\lambda = 1.5418 \text{ \AA}$). N₂ adsorption-desorption isotherms were obtained using a Micromeritics TriStar 3000 analyzer. ATR-FTIR spectra were recorded on a Perkin-Elmer Spectrum Two FT-IR spectrometer (4000 to 400 cm⁻¹). Photoluminescence (PL) spectra were acquired with a Perkin Elmer FL 8500 fluorescence spectrometer. A Perkin-Elmer LAMBDA 850+ spectrophotometer was used to obtain DRUV-vis diffuse reflectance spectra. Transmission electron microscopy (TEM) images were collected using a JEOL F200 electronic microscope at 200 kV and field-emission scanning electron microscopy (FESEM) images were obtained using a JEOL (JSM 7900F) scanning microscope at 10 kV. Electrochemical measurements were conducted using a potentiostat/galvanostat (Autolab PSGTAT302) equipped with an impedance module. The measurements were carried out with a carbon-paste-modified electrode as the working electrode (WE), containing 10 wt% of active material in commercial carbon paste and using Nujol as an agglutinant. Cyclic voltammetry (CV) and differential pulse voltammetry (DPV) were measured in an aqueous solution of Na₂SO₄ (0.2 M) as the electrolyte, with a platinum rod as the counter electrode (CE) and an Ag/AgCl/KCl (3 M) electrode as the reference electrode (RE). Electrochemical impedance spectroscopy (EIS) measurements were performed using a similar setup, with an SCE as the RE and 0.2 M KOH as the electrolyte. Photocurrent experiments were conducted on a drop-cast glassy carbon electrode as the WE. The ink drop-cast onto the commercial glassy carbon electrode contained 5 mg of commercial Ketjenblack carbon and 3 mg of active material suspended in a mixture of 500 μL of Milli-Q water, 500 μL of ethanol, and 20 μL of Nafion. A 6 μL aliquot of the resulting mixture was drop-cast onto the electrode and left to air dry. Then, the electrode was introduced into an aqueous solution of 0.2 M Na₂SO₄ as the electrolyte, with a platinum plaque as the CE, and Ag/AgCl/KCl (3 M) as the RE. The electrode was exposed to light for periods of 20 s, followed by 10 s of darkness.

2.4. Photocatalytic experiments

The photocatalytic activity of the Bi₂O₂CO₃-based samples was evaluated for degrading contaminants in Milli-Q water

and tap water. Two antibiotics, ciprofloxacin (CIP) and sulfamethoxazole (SMZ), and a UVA filter (BP-4) were chosen as target persistent contaminants. In a typical experiment, 20 mg of the bismuth-based sample was added to 20 mL of an aqueous solution containing the contaminant (15 mg L⁻¹ of CIP and 10 mg L⁻¹ for SMZ and BP-4). The suspension was stirred in the dark for 30 min to ensure the adsorption-desorption equilibrium has been reached. Subsequently, the suspension was irradiated using a 300 W Xe lamp. An aliquot was taken at different periods, and the resulting liquid was analyzed by UV-vis spectroscopy or HPLC. The concentration of CIP was determined by monitoring the change in absorbance at 272 nm, while the concentrations of SMZ and BP-4 were calculated by HPLC (Perkin Elmer LC300 system with a C18 reverse-phase column (4.4 μm , 4.6 \times 100 mm) equipped with a multiwavelength UV-vis detector at wavelengths of 262 nm and 227 nm for SMZ and BP-4, respectively). SMZ concentration was determined using an isocratic method with a 70:30 (water (0.1% formic acid): methanol) solvent system and oven temperature of 30 °C. BP-4 concentration was determined with a solvent system of acetonitrile and acetic acid (1 mM) in water (30:70). The retention times were 8.03 and 3.78 min for SMZ and BP-4, respectively.

The total organic carbon (TOC) was measured for the fresh contaminant solution (TOC_{initial}) and the resulting solution after the degradation experiment (TOC_{final}) at different reaction times: 30 min, 60 min and 180 min, for CIP, SMZ and BP-4, respectively. The mineralization rates were calculated by determination of TOC using a combustion/non-dispersive infrared gas analyzer model TOC-V from Shimadzu and the following equation:

$$\% \text{ Mineralization} = \frac{\text{TOC}_{\text{initial}} - \text{TOC}_{\text{final}}}{\text{TOC}_{\text{initial}}} \times 100$$

Electron paramagnetic resonance (EPR) spectra were acquired using an EMXmicro spectrometer (Bruker). To detect hydroxyl and superoxide radicals, 50 mg of the sample was dispersed in 1 mL of water or methanol, respectively, with 5,5-dimethyl-1-pyrroline N-oxide (DMPO) as the spin-trapping agent. Then, the dispersion was irradiated under UV light (xenon lamp, 300 W) for 20 min.

3. Results and discussion

3.1. Synthesis and characterization of Bi₂O₂CO₃-based samples

The morphology of Bi₂O₂CO₃ can be modified using various synthetic methods, including templated and not templated approaches²⁷ as previously reported. In this work, we present a novel and straightforward alternative method to prepare, for the first time, Bi₂O₂CO₃ nanosheets using choline hydroxide (CholOH) as a structure-directing agent, followed by heat treatment at 260 °C for 4 h. This optimal temperature



was chosen to ensure the thermal decomposition of CholOH (occurring at *ca.* 175 °C)²⁸ while preventing the formation of Bi₂O₃ (occurring at temperatures higher than 280 °C).²⁶ By adjusting the amount of CholOH (*i.e.* 5%, 10% and 20 wt%), the materials denoted as Chol5%-Bi₂O₂CO₃, Chol10%-Bi₂O₂CO₃ and Chol20%-Bi₂O₂CO₃ were obtained.

The phase composition of the prepared materials was confirmed by PXRD patterns, as shown in Fig. 1. The diffraction patterns for both Bi₂O₂CO₃ and CholX%-Bi₂O₂CO₃ samples matched the standard tetragonal phase of Bi₂O₂CO₃ (JCPDS No. 41-1488), indicating that the use of CholOH did not notably alter the crystal structure of Bi₂O₂CO₃. The absence of additional peaks in any of the diffractograms confirmed the high purity of the as-prepared samples. Additionally, an increase of CholOH amount led to a slight shift of the (013) and (110) peaks towards higher angles (2θ) (Fig. S1†) suggesting slight changes in the Bi₂O₂CO₃ lattice. This observation is consistent with the calculated lattice parameters, which revealed a reduction of the unit cell (*i.e.* cell volume from 213.65 to 204.81 Å³ and *c*-unit cell parameter from 13.97 to 13.78 Å) with an increase of CholOH, suggesting the existence of OVs (Table 1). This observation aligns with other studies,²⁹ where oxygen vacancies led to lattice contraction. The crystallite size was calculated by applying Scherrer's equation to the (013) plane diffraction peak (Table 1). It was observed that the crystallite size decreases upon the addition of CholOH in comparison to bare Bi₂O₂CO₃, and from this point, it increases gradually with the amount of structure-directing agent. In this context, it seems plausible that while CholOH facilitates the formation of smaller crystallites at lower concentrations, higher CholOH amounts may promote particle growth due to increased structure-directing effects. Therefore, CholOH seems to play a crucial role in modulating the crystal structure and crystallite size of Bi₂O₂CO₃, while also promoting the formation of OVs.

To further confirm the removal of [Chol]⁺ moieties in the Bi₂O₂CO₃-modified nanosheets, FTIR and ¹³C-MAS-NMR

spectra were recorded. The FTIR spectra (Fig. 2a) show the characteristic bands attributed to the CO₃²⁻ anions orthogonally inserted within [Bi₂O₂]²⁺ layers, which are present in all the studied samples. The bands at 1456 cm⁻¹ and 1382 cm⁻¹ correspond to anti-symmetric vibration v_3 , while the band at 845 cm⁻¹ corresponds to out-of-plane bending mode v_2 of CO₃²⁻.³⁰ Moreover, the peaks at 1067 cm⁻¹ and 691 cm⁻¹ are assigned to symmetric stretching modes v_1 , and in-plane deformation v_4 of CO₃²⁻, respectively. The characteristic Bi–O band appears at 549 cm⁻¹.³¹ Significantly, in the spectra of CholX%-Bi₂O₂CO₃ materials new broad bands appear at 3600–3200 cm⁻¹ and at 1640 cm⁻¹, which correspond to O–H stretching and bending vibration of physisorbed water molecules, respectively. The appearance of these bands for CholX%-Bi₂O₂CO₃ materials suggests the presence of hydrogen bonding between water molecules and the OVs (*i.e.*, defective O²⁻/O⁻) from [Bi₂O₂]²⁺ layers. It is important to note that no characteristic bands of the [Chol]⁺ moieties appear in the spectra, suggesting their complete removal by thermal treatment. To confirm this observation, FTIR spectra of CholOH and Chol20%-Bi₂O₂CO₃ were recorded before calcination (Fig. S2†) and the spectra showed the bands of the [Chol]⁺ moieties appearing at 1467 and 1523 cm⁻¹ in the spectrum of Chol20%-Bi₂O₂CO₃ before calcination treatment, which disappear after calcination treatment. The ¹³C MAS-NMR spectra (Fig. 2b) provide additional confirmation of the removal of [Chol]⁺ moieties. All samples show a broad peak at δ = 167 ppm, attributed to interlayered carbonate anions. Interestingly, a signal at δ = 56 ppm is observed in the spectrum of Chol20%-Bi₂O₂CO₃, which can be attributed to methylene carbon atoms.³² This suggests that the partial thermal decomposition of [Chol]⁺ moieties may result in methylene groups within the Bi₂O₂CO₃ structure.

To gain further insights into the chemical composition of Bi₂O₂CO₃-based materials, high-resolution XPS measurements were conducted for Bi₂O₂CO₃ and Chol10%-Bi₂O₂CO₃, as representative samples. The full-scan XPS spectra reveal the presence of oxygen (O 1s), carbon (C 1s) and bismuth (Bi 4f) in both samples (Fig. 3a). The XPS spectrum of Bi 4f for Bi₂O₂CO₃ (Fig. 3b) displays a doublet corresponding to Bi 4f_{5/2} (164.1 eV) and Bi 4f_{7/2} (158.9 eV), which is characteristic of Bi³⁺ species in the [Bi₂O₂]²⁺ layers.³³ In contrast, in the spectrum of Chol10%-Bi₂O₂CO₃, the Bi 4f doublet can be deconvoluted into four peaks. Two less intense peaks (158.4 and 163.6 eV) are observed to shift to lower binding energies compared to Bi₂O₂CO₃, supporting the presence of a lower valent bismuth state (*i.e.* Bi²⁺, 158.0 and 163.3 eV)³⁴ and/or the presence of OVs.³⁵ This evidence confirms the formation of surface OVs on the exterior of the [Bi₂O₂]²⁺ layers (Fig. S3†). The C 1s peak of the Bi₂O₂CO₃ material (Fig. 3c), associated with the CO₃²⁻ species, appears at 288.5 eV in the spectrum; this peak shifted slightly to 288.8 eV in Chol10%-Bi₂O₂CO₃ suggesting that the electronic density of C in the CO₃²⁻ layers has been slightly modified.³⁶

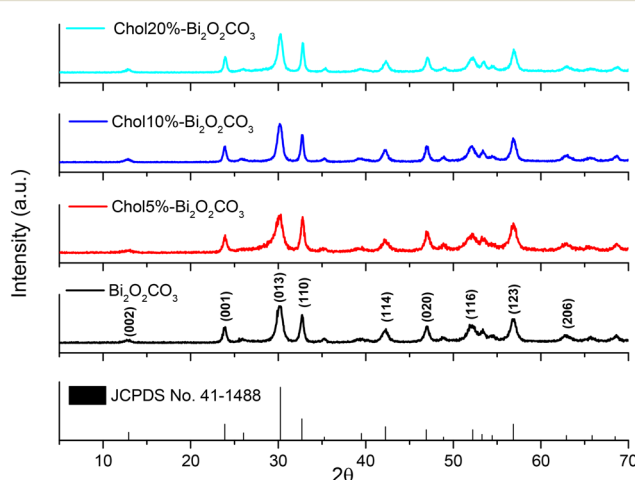


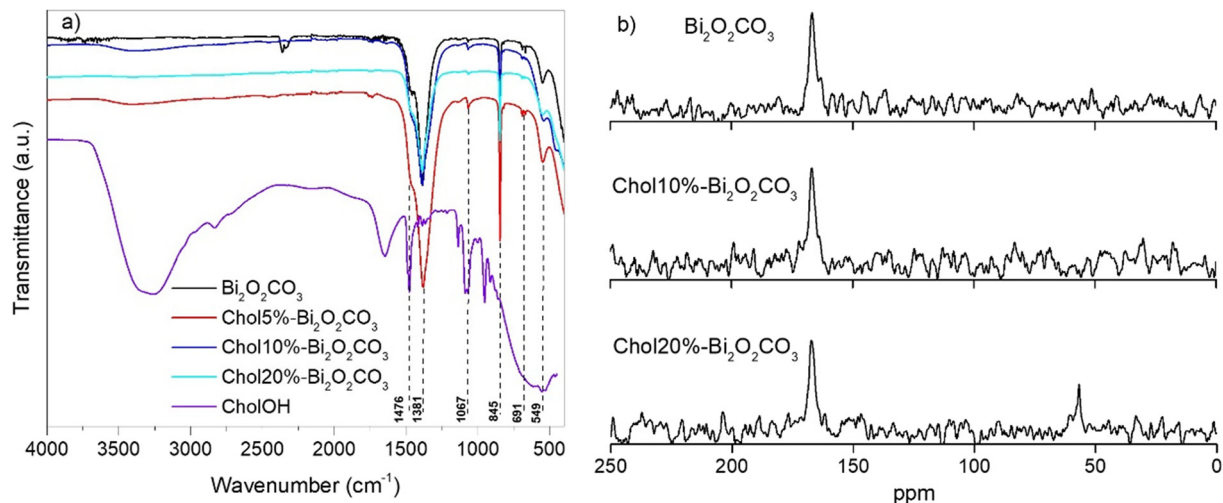
Fig. 1 PXRD patterns of the Bi₂O₂CO₃-based samples.



Table 1 Specific surface areas (S_{BET}), band gap values, crystallite sizes and lattice parameters of $\text{Bi}_2\text{O}_2\text{CO}_3$ samples

Material	S_{BET} ($\text{m}^2 \text{ g}^{-1}$)	Band gap ^a (eV)	Crystallite size ^b (nm)	Lattice parameters		
				$a = b$ (Å)	c (Å)	V (Å ³)
$\text{Bi}_2\text{O}_2\text{CO}_3$	11.52	3.32	19.18	3.91	13.97	213.65
Chol5%- $\text{Bi}_2\text{O}_2\text{CO}_3$	12.26	3.29	11.93	3.86	13.86	206.45
Chol10%- $\text{Bi}_2\text{O}_2\text{CO}_3$	22.49	3.32	13.13	3.86	13.78	205.66
Chol20%- $\text{Bi}_2\text{O}_2\text{CO}_3$	12.27	3.24	16.67	3.86	13.78	204.81

^a Estimated by the application of the Kubelka–Munk function. ^b Calculated by Scherrer's equation.

Fig. 2 a) FTIR spectra of the $\text{Bi}_2\text{O}_2\text{CO}_3$ -based materials and b) ¹³C MAS NMR spectra of $\text{Bi}_2\text{O}_2\text{CO}_3$, Chol10%- $\text{Bi}_2\text{O}_2\text{CO}_3$ and Chol20%- $\text{Bi}_2\text{O}_2\text{CO}_3$.

An additional C 1s peak at 284.8 eV can also be deconvoluted into two signals at 284.8 and 285.6 eV, which were assigned to adventitious carbon species. In the C 1s spectrum of Chol10%- $\text{Bi}_2\text{O}_2\text{CO}_3$, an additional peak is also observed at 283.7 eV, which could be attributed to the presence of residual carbon from the partial thermal decomposition of $[\text{Chol}]^+$ moieties.³⁷ The O 1s spectra for $\text{Bi}_2\text{O}_2\text{CO}_3$ and Chol10%- $\text{Bi}_2\text{O}_2\text{CO}_3$ (Fig. 3d) were deconvoluted into three distinct peaks, at 529.6, 530.6 and 531.4 eV. These peaks correspond to the Bi–O bond in $[\text{Bi}_2\text{O}_2]^{2+}$, the C–O bond in CO_3^{2-} and OVs,³⁸ respectively. Notably, the intensity of the peak at 531.4 for Chol%- $\text{Bi}_2\text{O}_2\text{CO}_3$ (13.6%) is higher in comparison to $\text{Bi}_2\text{O}_2\text{CO}_3$ (5.5%), supporting the hypothesis that the use of choline hydroxide, as a structure-directing agent, induces the generation of additional OVs, which are known to play a crucial role in enhancing the photocatalytic performance of the material.

The morphology of the samples was examined by FESEM and TEM (Fig. 4). According to the FESEM images, both samples are composed of irregular nanosheets with a slight decrease in the size of the Chol10%- $\text{Bi}_2\text{O}_2\text{CO}_3$ sample (Fig. 4b) in comparison with unmodified $\text{Bi}_2\text{O}_2\text{CO}_3$ (Fig. 4a). Remarkably, TEM images show that the surface of the material was significantly modified by CholOH treatment as evidenced by the presence of rounded edges in the Chol10%- $\text{Bi}_2\text{O}_2\text{CO}_3$ sample (Fig. 4d).

A high specific surface area is crucial for enhancing the adsorption capacity of materials. To assess this, N_2 adsorption–desorption isotherms were measured for $\text{Bi}_2\text{O}_2\text{CO}_3$ -based materials. All isotherms correspond to type III of the IUPAC classification, featuring an H3 hysteresis loop (Fig. S4†). It is important to highlight that Chol10%- $\text{Bi}_2\text{O}_2\text{CO}_3$ displayed the highest specific surface area, which was twice that of pure $\text{Bi}_2\text{O}_2\text{CO}_3$ (22.49 vs. $11.52 \text{ m}^2 \text{ g}^{-1}$) and slightly higher than other recently reported modified $\text{Bi}_2\text{O}_2\text{CO}_3$ materials such as N-doped $\text{Bi}_2\text{O}_2\text{CO}_3$ (ref. 39) ($S_{\text{BET}} = 17.13 \text{ m}^2 \text{ g}^{-1}$), $\text{Bi}_2\text{O}_2\text{CO}_3/\text{BOI}-0.5$ (ref. 40) ($S_{\text{BET}} = 15.63 \text{ m}^2 \text{ g}^{-1}$) and $\text{Bi}_2\text{O}_2\text{CO}_3$ PS ($S_{\text{BET}} = 13.87 \text{ m}^2 \text{ g}^{-1}$).⁴¹ This result indicates that using the appropriate amount of CholOH as a structure-directing agent significantly improves the surface area.

The photoluminescence and optical properties of the $\text{Bi}_2\text{O}_2\text{CO}_3$ -based materials were analyzed using PL and DRUV-vis spectroscopy. All samples showed an absorption band which appears in the UV region (Fig. S5a†). Therefore, $\text{Bi}_2\text{O}_2\text{CO}_3$ is classified as a direct semiconductor (n-type), thus, the band gap values were estimated using the Kubelka–Munk method, ranging from 3.24 to 3.32 eV (Fig. S5b,† Table 1). The PL spectra (Fig. S6†) revealed that bare $\text{Bi}_2\text{O}_2\text{CO}_3$ exhibited the highest band intensity, while Chol10%- $\text{Bi}_2\text{O}_2\text{CO}_3$ showed the lowest, indicating better separation efficiency of photogenerated electron–hole pairs in the modified system (Chol10%- $\text{Bi}_2\text{O}_2\text{CO}_3$).



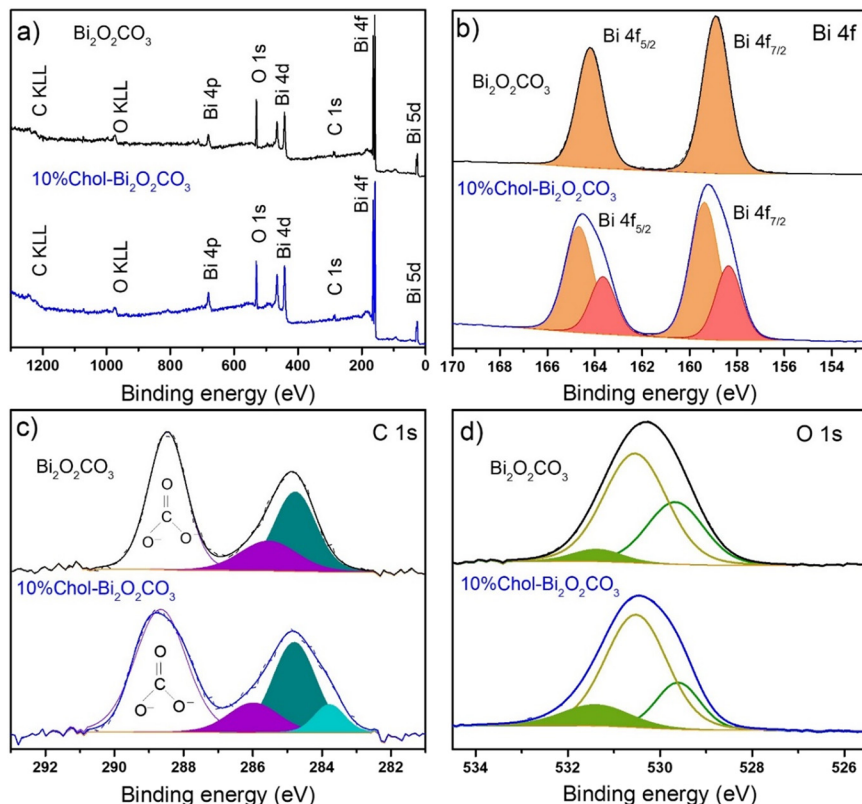


Fig. 3 XPS for $\text{Bi}_2\text{O}_2\text{CO}_3$ and Chol10%- $\text{Bi}_2\text{O}_2\text{CO}_3$ samples: a) survey spectra, b) Bi 4f region, c) C 1s region and d) O 1s region.

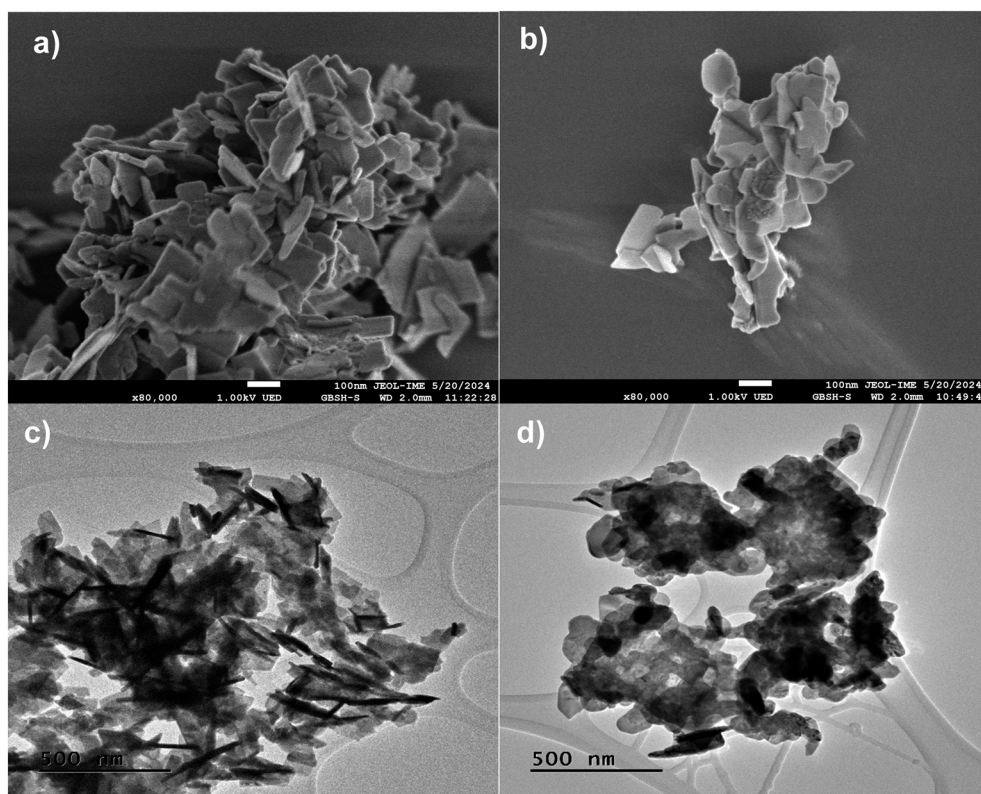


Fig. 4 FESEM images of a) $\text{Bi}_2\text{O}_2\text{CO}_3$ and b) Chol10%- $\text{Bi}_2\text{O}_2\text{CO}_3$. TEM images of c) $\text{Bi}_2\text{O}_2\text{CO}_3$ and d) Chol10%- $\text{Bi}_2\text{O}_2\text{CO}_3$.

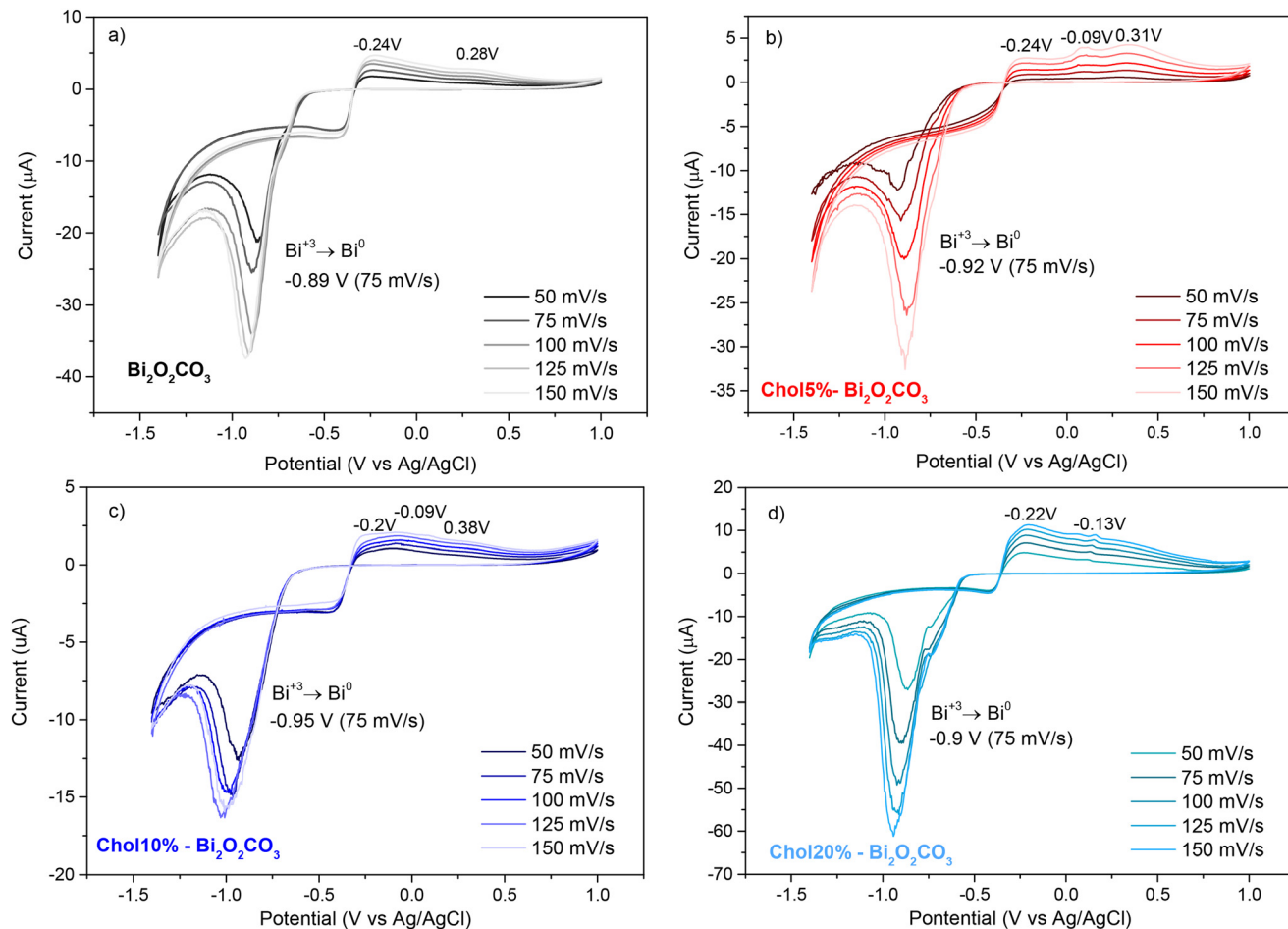
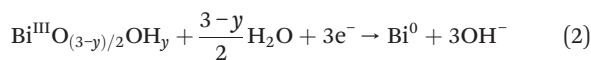
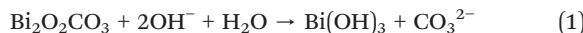


Fig. 5 CV for $\text{Bi}_2\text{O}_2\text{CO}_3$ -based samples in Na_2SO_4 (0.2 M) measured between -1.4 and 1.0 V (V vs. Ag/AgCl/KCl) a) $\text{Bi}_2\text{O}_2\text{CO}_3$, b) Chol5%- $\text{Bi}_2\text{O}_2\text{CO}_3$, c) Chol10%- $\text{Bi}_2\text{O}_2\text{CO}_3$ and d) Chol20%- $\text{Bi}_2\text{O}_2\text{CO}_3$.

In addition, the electrochemical properties of the samples were examined by cyclic voltammetry (CV) and differential pulse voltammetry (DPV). The CV curves for $\text{Bi}_2\text{O}_2\text{CO}_3$ -modified carbon paste electrodes (CPE) (Fig. 5a) exhibited a cathodic peak associated with the reduction of $\text{Bi}^{(III)}$ to Bi^0 at a scan rate of 50 mV s^{-1} . As the scan rate increases, the cathodic peak shifted to more negative potentials and the peak current increased, indicating excellent rate performance of the $\text{Bi}_2\text{O}_2\text{CO}_3$ electrode, and rapid faradaic reactions. In alkaline media, $\text{Bi}_2\text{O}_2\text{CO}_3$ undergoes partial dissolution as shown in eqn 1. Thus, the first step before the cathodic process involves the partial dissolution of bismuth species $[\text{Bi}_2\text{O}_2]^{2+}$ into the ionic species $\text{BiO}_2^-(\text{aq})$, followed by its reduction to Bi^0 through successive reactions involving different bismuth oxidation states. So, in the CV curve, the broad reduction peak at -0.89 V is associated with the reduction of dissolved Bi^{3+} species, representing the global process shown in eqn (2)



During the anodic scan, a crossover is observed, which is a reliable diagnostic tool for confirming the formation of bismuth metal on the electrode surface. A shift in the oxidation potential occurs, indicating that it is close to the metal/metal ion equilibrium potential. This is because the oxidation of metallic bismuth initiates from the material deposited on the surface of the electrode. Anodic potential scans revealed two anodic peaks at -0.24 and 0.28 V, the latter being followed by a quasi-horizontal plateau. This behaviour is consistent with the oxidation of Bi^0 located at the surface/solution interface together with the oxidation of Bi^0 farther from the surface. In both cases, the underlying mechanism involves the oxidation of Bi^0 to Bi^+ and the disproportionation of Bi^+ to Bi^{3+} and Bi^0 (eqn (3) and (4)). In a carbonate solution, Bi^{3+} reacts with OH^- to form $\text{Bi}(\text{OH})_3/\text{BiOOH}$, which subsequently evolves in an alkaline medium according to eqn (5).⁴²





The CV curves for CholX%-Bi₂O₂CO₃ materials (Fig. 5b-d) show that the main cathodic peak is slightly shifted to lower (more negative) potentials compared to unmodified Bi₂O₂CO₃ (e.g., -0.95 V vs. -0.89 V for Chol10%-Bi₂O₂CO₃ and Bi₂O₂CO₃, respectively). This shift is due to the more abundant OVs, in Chol10%-Bi₂O₂CO₃, which facilitate the reduction potential of Bi³⁺ at lower potentials (more negative). In addition, during the anodic scans, new oxidation peaks, attributed to the oxidation of Bi⁰ species, were observed for CholX%-Bi₂O₂CO₃ samples confirming the XPS analysis results regarding the increased density of OVs in the modified nanosheets.

The results obtained in CV studies are consistent with those obtained by DPV measurements. The DPV for unmodified Bi₂O₂CO₃ (Fig. 6a) shows one main peak attributed to BiO₂⁻(aq) in solution, as previously discussed. In the DPV curves for CholX%-Bi₂O₂CO₃ materials (Fig. 6b-d), a new peak is observed, which is attributed to BiO₂⁻(ads) adsorbed species. Similar peaks, at higher potentials, have

been attributed to the presence of BiO₂⁻(ads) adsorbed species, in CV studies for Bi₂O₃.⁴³ DPV can also be utilized to assess the electrochemical ion exchange performance of these electrodes in the electrolyte solution. Applying a reduction potential to the electrode, the bismuth material gains a negative charge. Consequently, sodium cations from the electrolyte (0.2 M Na₂SO₄) are presumably absorbed into the material to neutralize this negative charge. As mentioned above, Bi₂O₂CO₃-based materials show substantial cathodic peaks of Bi(III) species, which may also result in the incorporation of sodium cations. According to the DPV curves, it becomes clear that the Chol10%-Bi₂O₂CO₃ electrode shows a significantly larger redox peak area and higher current values than the others, demonstrating superior electrochemical performance and improved ion exchange performance for sodium cations. This suggests that Chol10%-Bi₂O₂CO₃ may have more active sites for redox reactions due to the presence of OVs and a higher adsorption capacity for positively charged molecules.

Electrochemical impedance spectroscopy (EIS) was conducted to evaluate the charge transfer kinetics at the interface between the Bi₂O₂CO₃-modified CPE and the electrolyte solution. Fig. 7a shows that all samples display

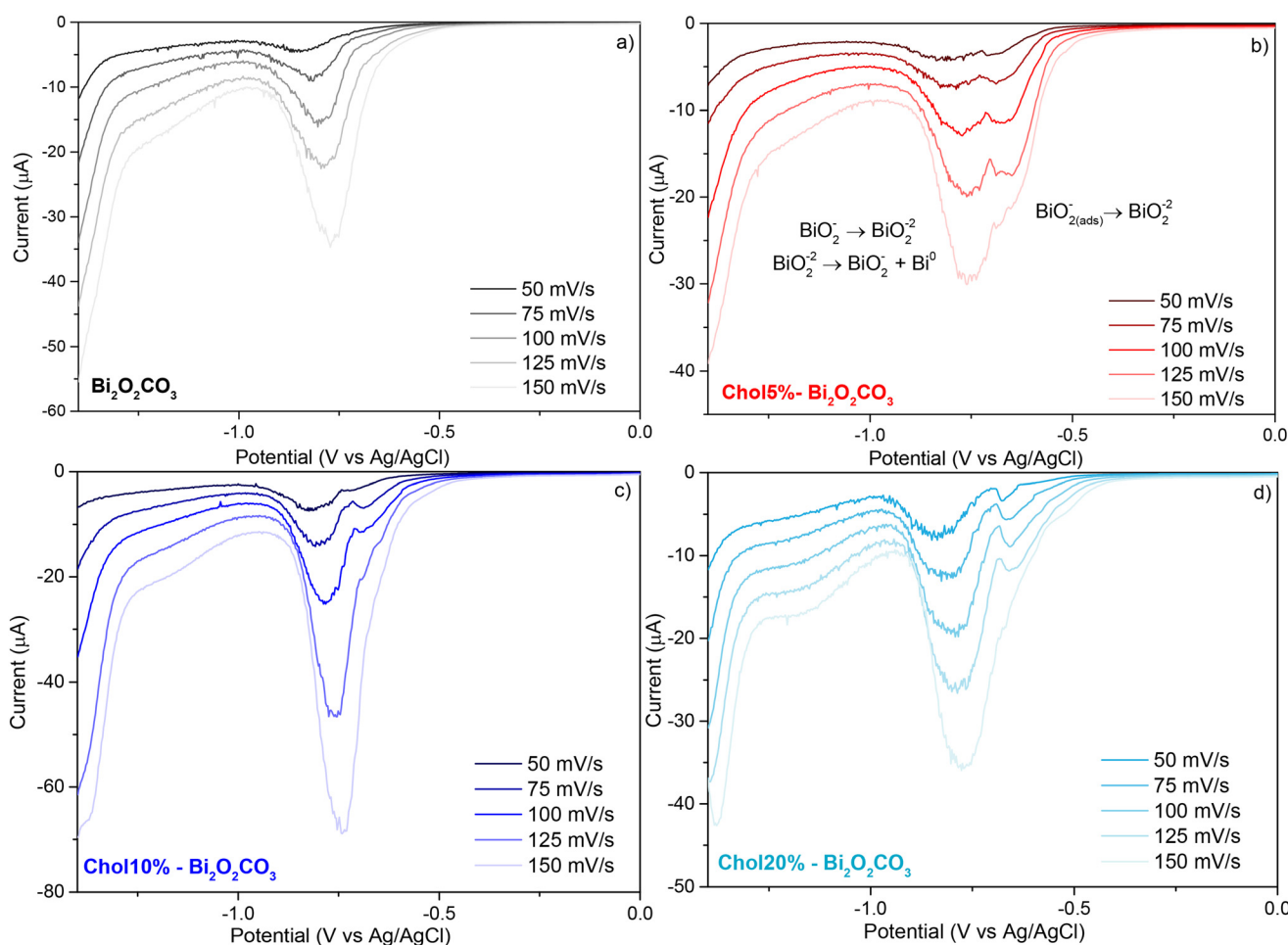


Fig. 6 DPV for Bi₂O₂CO₃-based samples in Na₂SO₄ (0.2 M) measured between -1.4 and 1.0 V (V vs. Ag/AgCl/KCl) a) Bi₂O₂CO₃, b) Chol5%-Bi₂O₂CO₃, c) Chol10%-Bi₂O₂CO₃ and d) Chol20%-Bi₂O₂CO₃.

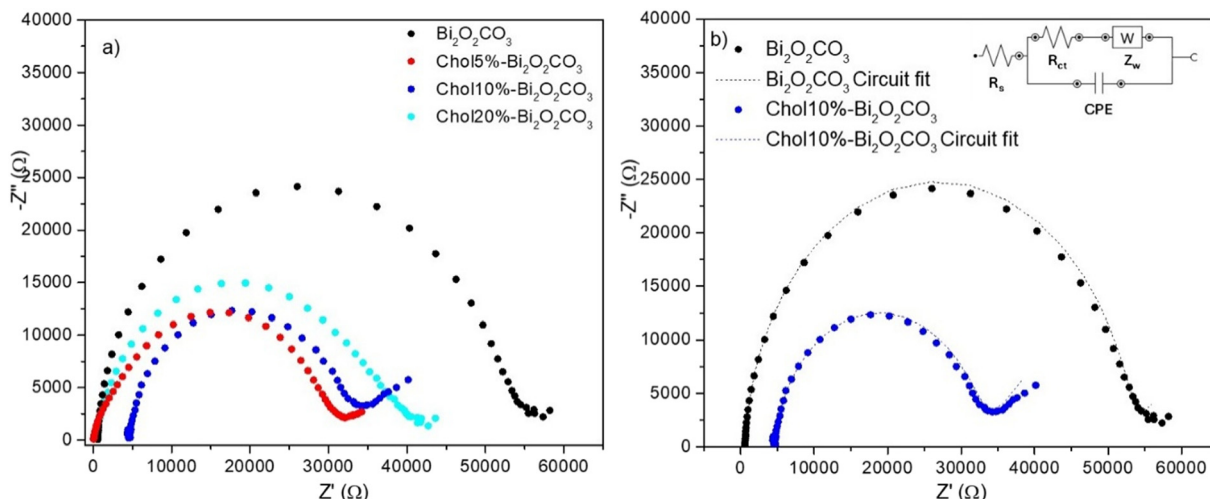


Fig. 7 a) EIS plots measured for $\text{Bi}_2\text{O}_2\text{CO}_3$ -based samples in KOH (0.2 M) from 0.1 to 60 000 Hz. b) Circuit fit of the EIS plots for Chol10%- $\text{Bi}_2\text{O}_2\text{CO}_3$ and $\text{Bi}_2\text{O}_2\text{CO}_3$.

well-defined semicircles, indicating that the charge-transfer resistance is the dominant factor controlling the process. Notably, $\text{Bi}_2\text{O}_2\text{CO}_3$ -modified materials, with 5% and 10% of ionic liquid, exhibit a minor linear slope, suggesting that an incorporation of the appropriate amount of the ionic liquid in the material enhances the diffusion processes taking place at the electrode-electrolyte interface. Furthermore, the smaller semicircle radii in the modified materials indicate that all choline-based systems and specially Chol10%- $\text{Bi}_2\text{O}_2\text{CO}_3$ possess lower resistance and more efficient charge transfer compared to bare $\text{Bi}_2\text{O}_2\text{CO}_3$, which aligns well with the results and conclusions taken from DPV analysis. Additionally, an equivalent Randles model circuit was fitted for both bare $\text{Bi}_2\text{O}_2\text{CO}_3$ and Chol10%- $\text{Bi}_2\text{O}_2\text{CO}_3$. The equivalent circuit model consists of four elements R_s , R_{ct} , CPE, and Z_w (Fig. 7b). R_s represents the resistance of the electrolyte between the reference and working electrodes and R_{ct} reflects the resistance to the transfer of electrons at the electrode/electrolyte interface. CPE or constant phase element is used to model non-ideal capacitance behavior arising from factors such as surface roughness, non-uniformity or surface porosity of the electrode and Z_w or Warburg impedance is a result of diffusion processes taking place at the electrode-electrolyte interface⁴⁴. R_{ct} values are 28 k Ω and 52 k Ω for Chol10%- $\text{Bi}_2\text{O}_2\text{CO}_3$ and $\text{Bi}_2\text{O}_2\text{CO}_3$, respectively (Table S2†). The lower R_{ct} value for Chol10%- $\text{Bi}_2\text{O}_2\text{CO}_3$ indicates enhanced electronic and ionic conduction, factors that will notably boost the photocatalytic performance of this material.

To gain additional insights into the interfacial electron transfer dynamics, photocurrent experiments were conducted (Fig. S7†). The Chol10%- $\text{Bi}_2\text{O}_2\text{CO}_3$ sample exhibits a superior response compared to the other studied materials, indicating that more photo-induced electrons were generated by this system. This behavior supports a more effective separation of

photogenerated electron-hole pairs under UV-vis light. In contrast, Chol5%- $\text{Bi}_2\text{O}_2\text{CO}_3$ and $\text{Bi}_2\text{O}_2\text{CO}_3$ show similar response, while Chol20%- $\text{Bi}_2\text{O}_2\text{CO}_3$ exhibits the lowest response, again highlighting the influence of using an appropriate amount of ionic liquid in the preparation of the photocatalysts to improve their performance.

This electrochemical behavior together with the comprehensive characterization techniques employed previously consistently point to notable changes in the structural, optical, electronic, and electrochemical properties of the $\text{Bi}_2\text{O}_2\text{CO}_3$ -modified materials. The control of the ionic liquid concentration during the preparation of the nanosheets appears to be a critical factor in achieving optimal properties. In particular, the Chol10%- $\text{Bi}_2\text{O}_2\text{CO}_3$ sample exhibited a unique combination of enhanced surface area, modified chemical composition, and a high density of OVs. The synergy between structure, surface composition, and defect engineering highlights the potential of Chol10%- $\text{Bi}_2\text{O}_2\text{CO}_3$ as a promising candidate for application in photocatalytic degradation of pollutants. Therefore, these properties collectively will presumably contribute to its superior performance in photocatalytic processes.

3.2. Photocatalytic degradation of CIP by $\text{Bi}_2\text{O}_2\text{CO}_3$ -based samples

The photocatalytic activity of $\text{Bi}_2\text{O}_2\text{CO}_3$ -based samples was evaluated first using the antibiotic CIP as a model recalcitrant contaminant. As shown in Fig. 8a, all samples exhibited notable adsorption capacity for CIP (*i.e.*, 49.2–86.9%). The Chol10%- $\text{Bi}_2\text{O}_2\text{CO}_3$ sample demonstrated the highest adsorption capacity. It is well-established that adsorption capacity is significantly influenced by material characteristics such as specific surface area, crystalline size, morphological features, defects and surface charge, among others.⁴⁵ When comparing the zeta potential of the as-



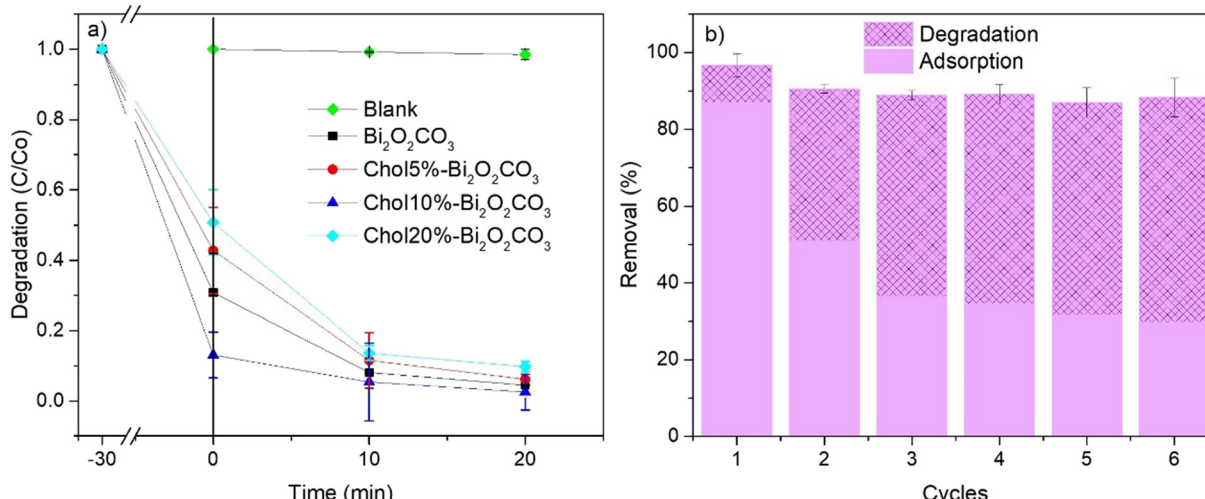


Fig. 8 a) Removal of CIP by Bi₂O₂CO₃-based materials and b) CIP removal by Chol10%-Bi₂O₂CO₃ during six consecutive photodegradation cycles.

prepared Bi₂O₂CO₃ materials (Table S3†), similar values were observed for all samples (ranging from -31.5 to -35.7), suggesting that surface charge does not play a significant role in CIP adsorption. Instead, the excellent adsorption capacity of Chol10%-Bi₂O₂CO₃ can be attributed principally to its higher specific surface area (22.49 vs. 11.52, 12.26 and 12.27 m² g⁻¹ for Bi₂O₂CO₃, Chol5%-Bi₂O₂CO₃ and Chol20%-Bi₂O₂CO₃, respectively). Moreover, its additional defects, such as OVs introduced in Chol10%-Bi₂O₂CO₃ further enhance its adsorption capability by presumably providing more active sites for CIP interaction.

Remarkably, the Chol10%-Bi₂O₂CO₃ sample demonstrated the highest CIP removal, achieving 97.5% within just 20 min (Table S3†). The CIP removal by Chol10%-Bi₂O₂CO₃ is higher compared to other reported Bi₂O₂CO₃-based samples (Table S1†) such as BOC-5 (ref. 46) (86.8% within 60 min) and Br₃-Bi₂O₂CO₃ (ref. 47) (95% within 30 min). In addition, Chol10%-Bi₂O₂CO₃ presents a higher removal capacity than TiO₂-based photocatalysts (TiO₂@PANI⁴⁸ and 0.4%Cu-0.5%S-TiO₂ (ref. 49) and composite-based photocatalysts (S-C₃N₄/ZnO, CeO₂-Ag/AgBr, Fe₃O₄/g-C₃N₄).⁵⁰⁻⁵²

The removal of pollutants through an adsorption process is widely considered a cost-efficient, environment friendly and straightforward method. In this context, the regeneration capacity is an essential factor in determining the feasibility and sustainability of the adsorbent. Regeneration processes, however, are often expensive and energy-intensive, requiring high temperatures vacuum conditions, microwave irradiation and or, frequently, the use of organic solvents.⁵³ Given the remarkable adsorption capacity of Chol10%-Bi₂O₂CO₃ (achieving CIP removal of 86.9% in 30 min), regeneration experiments were performed using Chol10%-Bi₂O₂CO₃ loaded with CIP. To carry out a sustainable regeneration process, the CIP-loaded sample was regenerated using a low-cost and green treatment consisting of washing the sample with a saturated NaHCO₃ solution for 30 min. After the

washing step, the regenerated Chol10%-Bi₂O₂CO₃ was suspended in a fresh CIP solution and the dispersion was stirred in the dark for 30 min. The resulting adsorption rate was 0.011 mg of CIP per mg of material, recovering around 88% of the initial CIP removal efficiency. To go further in the assessment of the reusability of the system, a second and third adsorption cycles were performed under similar conditions, achieving 88% and 83% efficiency, respectively. This performance, combined with its low-cost and green regeneration strategy, positions Chol10%-Bi₂O₂CO₃ as a promising adsorbent for sustainable water treatment applications.

The reusability of Chol10%-Bi₂O₂CO₃ was also investigated using a combination of adsorption and photocatalytic processes (30 min in the dark and 30 min under UV-vis irradiation), without further treatment. As shown in Fig. 8b, while the CIP removal by adsorption notably decreases after the first cycle, the CIP removal efficiency by Chol10%-Bi₂O₂CO₃ is maintained for at least 6 cycles owing to an increase in its photocatalytic activity. In other words, in the first run, CIP was mainly removed by adsorption (86.9% vs. 9.8%), whereas, by the sixth cycle, the photocatalytic degradation of the pollutant becomes the principal process (58.6% vs. 29.7%). Additionally, PXRD (Fig. S8†) and FT-IR analysis (Fig. S9†) confirmed the stability of Chol10%-Bi₂O₂CO₃, preserving its structure after 6 cycles. These results support the possibility of using Chol10%-Bi₂O₂CO₃ as a powerful dual-function adsorbent-photocatalyst.

3.3. Photocatalytic degradation of SMZ and BP-4 by Chol10%-Bi₂O₂CO₃

To further evaluate the performance of Chol10%-Bi₂O₂CO₃, its photocatalytic activity was also studied using the target contaminants sulfamethoxazole (SMZ) and benzophenone-4 (BP-4). The blank tests of SMZ and BP-4 resulted in negligible



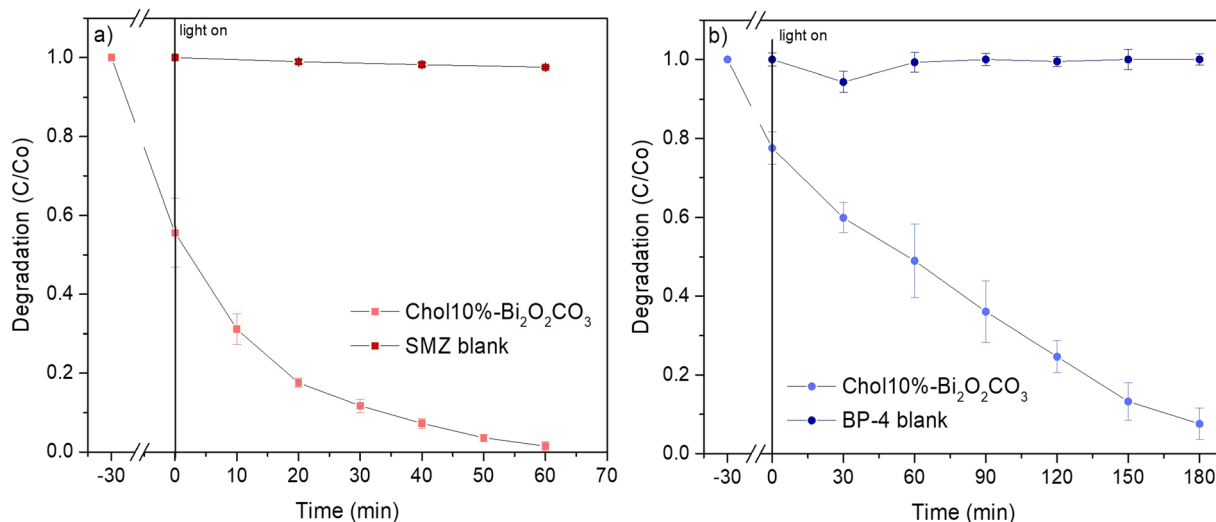


Fig. 9 Photocatalytic degradation of a) SMZ and b) BP-4 using Chol10%-Bi₂O₂CO₃.

degradation, indicating the need to use reactive oxygen species (ROS). In this regard, several authors have reported the efficient removal of SMZ through a photocatalytic process combining semiconductors (Table S1†). Herein, our as-prepared single semiconductor, Chol10%-Bi₂O₂CO₃, was able to eliminate 44.4% of SMZ in 30 min by adsorption to finally achieve a complete removal within the next 60 min under UV-vis light irradiation (Fig. 9a). This again demonstrates the promising adsorption and photodegradative ability of Chol10%-Bi₂O₂CO₃.

For BP-4 removal, it is important to highlight that Chol10%-Bi₂O₂CO₃ exhibited exceptional photodegradation performance in the absence of any additional oxidant, removing BP-4, almost completely, in 180 min (Fig. 9b). The kinetic constants (k) were calculated from a pseudo-first order reaction (Fig. S10†), resulting in a high-rate constant, $k = 0.053$ and $k = 0.014 \text{ min}^{-1}$, for the degradation of SMZ and BP-4, respectively. Comparing the photocatalyst performance of Chol10%-Bi₂O₂CO₃ with other reported photocatalysts, our material is able to remove SMZ faster than composites such as BiOBr/Bi₁₂O₁₇Br₂ (ref. 54) and AgBr-BaMoO₄ (ref. 55) with kinetic constants of 0.022 and 0.01 min^{-1} , respectively (Table S1†). Note here that the reported photocatalysts mentioned are composed of two semiconducting materials, in contrast to the simple semiconductor Chol10%-Bi₂O₂CO₃ reported here. Furthermore, the BP-4 removal by Chol10%-Bi₂O₂CO₃ (UV-vis, $k = 0.014 \text{ min}^{-1}$) is slightly higher than that of TiO₂-based nanowires⁵⁶ (UV-vis/H₂O₂, $k = 0.0129 \text{ min}^{-1}$) and slightly lower compared to that using the UV/chlorine method ($k = 0.02 \text{ min}^{-1}$).¹⁰

3.4. Photocatalytic degradation mechanisms and pathways

To deeply understand the degradation process of CIP, SMZ and BP-4 by Chol10%-Bi₂O₂CO₃, scavenger experiments were carried out using isopropanol (IPA), *p*-benzoquinone (BQ) and ascorbic acid (AA) as trapping agents for hydroxyl

radicals, superoxide radicals and holes, respectively (Fig. S11a†). For CIP degradation, holes are the main active species (efficiency drops from 98.8% to 39.2% in the presence of AA) and superoxide radicals are the secondary species (a 20% reduction in the removal in the presence of BQ), while hydroxyl radicals seem to not contribute to the process. For SMZ degradation, holes and superoxide radicals are also the primary and secondary reactive species, respectively, while hydroxyl radicals also play a role in the process (removal decreases from 92.4% to 62.5%). In contrast, BP-4 degradation is affected by the presence of all scavengers, with the degradation efficiency decreasing to 21.1%, 12.3% and 0% in the presence of IPA, AA and BQ, respectively. This indicates that for an efficient degradation of BP-4 the presence of holes, superoxide radicals and hydroxyl radicals is determinant and they all play an important role in the removal process. To confirm this, EPR measurements were carried out to detect hydroxyl ($\cdot\text{OH}$) and superoxide ($\cdot\text{O}_2^-$) radicals in Bi₂O₂CO₃ and Chol10%-Bi₂O₂CO₃ samples. For both samples, the peaks corresponding to $\cdot\text{OH}$ radicals were clearly observed after 20 min of UV irradiation, with the Chol10%-Bi₂O₂CO₃ sample exhibiting the highest intensity (Fig. S12a†). In contrast, the typical peaks associated with the DMPO- O_2^- adduct were not significantly detected in either sample (Fig. S12b†). Since photogenerated holes are involved in the formation of $\cdot\text{OH}$ radicals, both holes and $\cdot\text{OH}$ radicals are considered to play a major role in the photodegradation process for the Chol10%-Bi₂O₂CO₃ sample, as previously observed by scavenger experiments.

Additionally, the proposed degradation pathways for the three PPCPs were determined by HPLC/MS (Fig. S13, S15 and S17†). In the proposed degradation pathways of CIP (Fig. S14†), the CIP molecule undergoes a defluorination process ($m/z = 313$), followed by piperazine ring opening and loss of N atom ($m/z 300$).⁵⁷ The fragment could evolve through two possible approaches, both involving modifications to the



piperazine ring moieties, which generate the same mass ($m/z = 272$). CIP-4a could undergo transformation of the piperazine ring until the formation of a primary amine ($m/z = 244$)⁵⁸ or lose the carboxylic group of the quinoline ring, leading to the formation of CIP-6 ($m/z = 228$). The latter could lose the amino moiety (CIP-7) and undergo cleavage and opening of the quinolone and benzene rings.⁵⁹ Finally, the fragment continues its decomposition through the formation of malonic acid ($m/z = 104$) until mineralization ($\text{CO}_2 + \text{H}_2\text{O}$).⁶⁰

In addition, three possible degradation pathways are proposed for the degradation of SMZ (Fig. S16†). In the first pathway (I), the cleavage of the S–N bond of SMZ *via* the hydrolysis of the sulfonamide bond generates the degradation product SMZ-1 ($m/z = 99$). In contrast, in pathway II, SMZ could be converted to 2,4-dinitrobenzenesulfonic acid (SMZ-2) through consecutive ·OH attacks.⁶¹ A third possible pathway involves the cleavage of the isoxazole ring to give SMZ-3 ($m/z = 215$) initially, followed by the loss of the formamide group to form SMZ-5 ($m/z = 172$).⁶² An intermediate of SMX-3 undergoes loss of the amine group, giving 2-oxo-*N*-(phenyl sulfonyl) acetimidamide (SMZ-4) and the formamide group of SMZ-5 is oxidized to sulfonic acid (SMZ-6), which is eliminated in SMZ-7 ($m/z = 125$). Benzoic acid (SMZ-8) is transformed into maleic acid (SMZ-10) or phenol (SMZ-9), which can convert into malealdehyde (SMZ-12), resulting in benzene (SMZ-11). The last degradation intermediates consist of several molecules with diol groups (SMZ-13, SMZ-14 and SMZ-15).

Finally, the BP-4 degradation could follow two different pathways (Fig. S17†). In the first path, the reduction of the sulphonate group to a mercapto group leads to the formation of BP-4-1, which could be replaced by a hydroxyl group in the BP-4-2 intermediate and then evolves to BP-4-3.⁶¹ Pathway II starts with the cleavage of the molecule at the ketone group, oxidizing it to a carboxylic acid (BP-4-4). The latter could form two intermediates with the same m/z fragment (BP-4-5 and/or BP-4-6).⁷ BP-4-5 ($m/z = 218$) could generate also two possible new molecules (BP-4-7 and BP-4-8) depending on the reduction of one of the ketone groups. On the other hand, BP-4-6 leads to BP-4-9 ($m/z = 184$) by transforming all the functional groups of the ring and gives BP-4-10 or BP-4-11 when the formate group turns into a methoxy or a hydroxyl group, respectively. The last steps of the mechanism involve the loss of the hydroxyl groups from the phenyl ring (BP-4-12 and BP-4-13), the saturation of its bonds (BP-4-14) and its opening (BP-4-15) until the formation of the final fragment BP4-16 ($m/z = 62$).

The toxicity of degradation products was estimated using the Toxicity Estimation Software Tool (T.E.S.T) (Tables S4 and S5†), resulting in a low or no toxicity of the degradation intermediates. Furthermore, mineralization rates were determined for the three degradation experiments at optimized reaction times: 30 min, 60 min and 180 min, for CIP, SMZ and BP-4, respectively (Fig. S19†). The TOC removal efficiencies of the Chol10%– $\text{Bi}_2\text{O}_2\text{CO}_3$ photocatalyst were

remarkably high (83.3% mineralization for CIP, 75.5% for SMZ and 79.9% for BP-4), revealing its effectiveness in the photocatalytic degradation of these pollutants.

3.5. Photocatalytic degradation of CIP, SMZ and BP-4 in tap water

To further assess the applicability of Chol10%– $\text{Bi}_2\text{O}_2\text{CO}_3$ under realistic conditions, the degradation of three selected target contaminants (CIP, SMZ and BP-4) was tested in tap water from Madrid (Spain), which contains various anions and cations (see Table S6†). As shown in Fig. S11b,† complete removal of CIP was achieved in both Milli-Q and tap water, indicating that the presence of ions in tap water does not affect the degradation process of CIP. In contrast, the degradation efficiency of SMZ and BP-4 significantly decreased, from 98.5% to 18% and from 92.4% to 42%, from Milli-Q to tap water, respectively. This seems to be due to the presence of the inorganic anions that could trap the reactive species involved in the degradation process. In this regard, tap water contains ions such as chlorine (Cl^-), sulphate (SO_4^{2-}), and carbonate (CO_3^{2-}) (Table S6†), which have been described as scavengers of hydroxyl radicals.⁵⁹ As mentioned in the previous section, hydroxyl radicals seem to play a significant role only in the degradation SMZ and BP-4, but not in the elimination of CIP (Fig. S11a†), which supports the hypothesis of hydroxyl radicals being trapped by these ions present in tap water.

These results highlight the complexity of pollutant degradation in real water matrices and give an overview of the importance of understanding the interactions between inorganic ions and reactive oxygen species in the degradation of persistent pollutants in water. Despite these challenges, Chol10%– $\text{Bi}_2\text{O}_2\text{CO}_3$ shows a robust performance in removing CIP and seems to offer significant potential for the degradation of other contaminants in natural water systems.

To determine the valence band potential (E_{VB}) and conduction band potential (E_{CB}) for Chol10%– $\text{Bi}_2\text{O}_2\text{CO}_3$ and $\text{Bi}_2\text{O}_2\text{CO}_3$, EIS experiments were conducted. As expected,

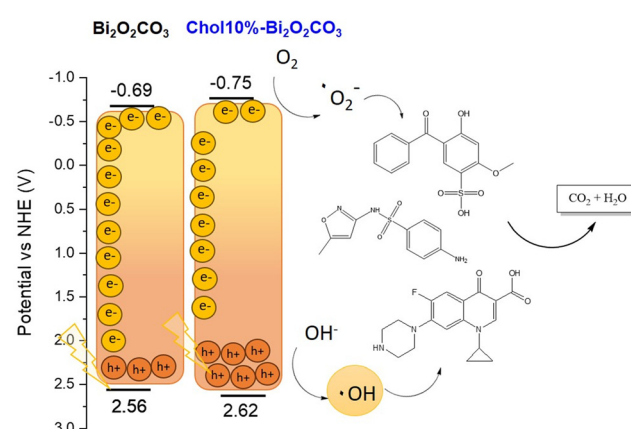


Fig. 10 Proposed mechanism for $\text{Bi}_2\text{O}_2\text{CO}_3$ and Chol10%– $\text{Bi}_2\text{O}_2\text{CO}_3$.



Mott–Schottky plots of both materials exhibit positive slopes (Fig. S20†), confirming their classification as n-type semiconductors. The flat band potential was determined from the intersection of the plot with the x -axis, resulting in values of -1.44 and -1.55 V vs. Ag/AgCl (equivalent to -0.80 and -0.86 V vs. NHE) for $\text{Bi}_2\text{O}_2\text{CO}_3$ and Chol10%– $\text{Bi}_2\text{O}_2\text{CO}_3$, respectively.

For n-type semiconductors, the flat band potential typically aligns near the E_{CB} . Thus, the E_{CB} yielded values of -0.70 and -0.76 V, while E_{VB} values (estimated from $E_{\text{CB}} = E_{\text{VB}} - E_g$) were found to be 2.62 and 2.55 V for $\text{Bi}_2\text{O}_2\text{CO}_3$ and Chol10%– $\text{Bi}_2\text{O}_2\text{CO}_3$, respectively. These shifts in the E_{CB} and E_{VB} bands might be influenced by the introduction of choline hydroxide. A proposed mechanism for both materials is illustrated in Fig. 10.

According to the results, the superior photocatalytic performance of Chol10%– $\text{Bi}_2\text{O}_2\text{CO}_3$ seems to rely on three main factors: i) its larger surface area, which enhances adsorption capacity and increases the number of active sites for photocatalysis; ii) its high density of OVs, which facilitates charge transfer and reduces the recombination of photogenerated charges; and iii) its enhanced electronic and ionic conductivity and boosted photocurrent activity which helps in the improvement of the photocatalytic efficiency.

4. Conclusions

For the first time, $\text{Bi}_2\text{O}_2\text{CO}_3$ nanosheets were successfully synthesized using choline hydroxide as a structure-directing agent for water remediation. Due to the higher concentration of OVs, Chol10%– $\text{Bi}_2\text{O}_2\text{CO}_3$ exhibited more efficient charge transfer and enhanced charge separation compared to pristine $\text{Bi}_2\text{O}_2\text{CO}_3$, as evidenced by DPV, EIS and PL measurements. These properties highlight the potential of Chol10%– $\text{Bi}_2\text{O}_2\text{CO}_3$, as a functional material capable of acting both as an adsorbent and a photocatalyst for the degradation of various PPCPs, including CIP (97.5% in 20 min), SMZ (98.5% in 60 min) and BP-4 (92.4% in 180 min), in the absence of any additional oxidant. This performance surpasses many other bismuth-based materials reported in the literature.

The comprehensive mechanistic study of the degradation of pollutants in water using Chol10%– $\text{Bi}_2\text{O}_2\text{CO}_3$ revealed that the position of energy bands of this material and the experiments with trapping agents make this material capable of generating both hydroxyl and superoxide radicals. This capability offers a significant advantage over other bismuth-based materials, as it allows to produce a greater variety of reactive oxygen species (especially hydroxyl and superoxide radicals, confirmed by scavenger experiments), thereby enhancing its photocatalytic activity and potential. In this sense, the TOC removal was exceptionally high, 83.3% mineralization for CIP, 75.5% for SMZ and 79.9% for BP-4.

Furthermore, Chol10%– $\text{Bi}_2\text{O}_2\text{CO}_3$ has demonstrated to be a robust material, with outstanding stability (confirmed by different techniques) and excellent reusability for at least 6

consecutive degradation cycles. These results position Chol10%– $\text{Bi}_2\text{O}_2\text{CO}_3$ as a reliable material for long-term photocatalytic applications.

Data availability

The data supporting this article have been included as part of the ESI.†

Author contributions

Helena Pérez del Pulgar: writing – original draft, methodology, investigation, conceptualization. Josefa Ortiz-Bustos: methodology, investigation. Santiago Gómez-Ruiz: writing – review & editing, funding acquisition. Isabel del Hierro: writing – review & editing, supervision, methodology. Yolanda Pérez: writing – original draft, supervision, funding acquisition, conceptualization.

Conflicts of interest

The authors declare that they have no known competing financial interests or personal relationships that could have appeared to influence the work reported in this paper.

Acknowledgements

We would like to thank funding from the research project PID2022-136417NB-I00 financed by Agencia Estatal de Investigación–Ministerio de Ciencia, Innovación y Universidades of Spain MCIU/AEI/10.13039/501100011033/ and “ERDF A way of making Europe”. We would also like to thank the support of Universidad Rey Juan Carlos to our research group COMET-NANO through the project M3271.

References

1. E. Emmanuel, M. G. Pierre and Y. Perrodin, *Environ. Int.*, 2009, **35**, 718–726.
2. L. Pan, J. Li, C. Li, X. Tang, G. Yu and Y. Wang, *J. Hazard. Mater.*, 2018, **343**, 59–67.
3. B. Liu, W. Liu, X. Nie, C. Guan, Y. Yang, Z. Wang and W. Liao, *J. Environ. Sci.*, 2011, **23**, 1558–1563.
4. D. G. J. Larsson, C. de Pedro and N. Paxeus, *J. Hazard. Mater.*, 2007, **148**, 751–755.
5. F. A. Kibuye, H. E. Gall, K. R. Elkin, B. Swistock, T. L. Veith, J. E. Watson and H. A. Elliott, *J. Environ. Qual.*, 2019, **48**, 1057–1066.
6. T. Simetić, J. Nikić, M. Kuč, D. Tamindžija, A. Tubić, J. Agbaba and J. Molnar Jazić, *Processes*, 2024, **12**(6), 1156.
7. R. Beel, C. Lütke Eversloh and T. A. Ternes, *Environ. Sci. Technol.*, 2013, **47**, 6819–6828.
8. Y. Huang, L. Luo, X. Y. Ma and X. C. Wang, *Environ. Sci. Pollut. Res.*, 2018, **25**, 32549–32561.
9. B. Imamović, P. Trebše, E. Omeragić, E. Bećić, A. Pečet and M. Dedić, *Molecules*, 2022, **27**(6), 1874.



10 L. Santbay, M. Kassir, R. Nassar, S. Mokh, M. Al Iskandarani and A. Rifai, *Environ. Sci. Pollut. Res.*, 2024, **31**, 31201–31212.

11 H. Liu, P. Sun, M. Feng, H. Liu, S. Yang, L. Wang and Z. Wang, *Appl. Catal., B*, 2016, **187**, 1–10.

12 M. Peng, E. Du, Z. Li, D. Li and H. Li, *Sci. Total Environ.*, 2017, **603–604**, 361–369.

13 X. Jia, J. Jin, R. Gao, T. Feng, Y. Huang, Q. Zhou and A. Li, *Chemosphere*, 2019, **222**, 494–502.

14 A. Ruz-Luna, M. Cruz-Yusta, M. Sánchez, L. Sánchez, B. Gámiz and I. Pavlovic, *J. Environ. Chem. Eng.*, 2024, **12**, 111709.

15 A. Chawla, A. Sudhaik, R. Sonu, P. Kumar, T. Raizada, A. Aslam Ahamad, P. Khan, Q. Van Le, V.-H. Nguyen, S. Thakur and P. Singh, *Coord. Chem. Rev.*, 2025, **529**, 216443.

16 A. Chauhan, R. Kumar, P. Raizada, S. Thakur, V.-H. Nguyen, A. Singh, Q. Van Le, P. Singh and A. Sudhaik, *Coord. Chem. Rev.*, 2025, **535**, 216634.

17 N. Shan, G. Liu, L. Li, J. Dong, B. Wang, M. Ji, H. Li and J. Xia, *J. Alloys Compd.*, 2024, **990**, 174202.

18 Q. Yang, J. Li, J. Zhong, C. Cheng, Z. Xiang and J. Chen, *Mater. Lett.*, 2017, **192**, 157–160.

19 L. Li, H. Gao, G. Liu, S. Wang, Z. Yi, X. Wu and H. Yang, *Adv. Powder Technol.*, 2022, **33**, 103481.

20 P. Chen, H. Liu, Y. Sun, J. Li, W. Cui, L. Wang, W. Zhang, X. Yuan, Z. Wang, Y. Zhang and F. Dong, *Appl. Catal., B*, 2020, **264**, 118545.

21 X. Guo, C. Liu, W. Hu, Z. Xu, L. Lu, C. Gao and X. Li, *Colloids Surf., A*, 2024, **685**, 133333.

22 Y. Feng, Z. Zhang, K. Zhao, S. Lin, H. Li and X. Gao, *J. Colloid Interface Sci.*, 2021, **583**, 499–509.

23 Y. Lu, Y. Huang, Y. Zhang, J. Cao, H. Li, C. Bian and S. C. Lee, *Appl. Catal., B*, 2018, **231**, 357–367.

24 X. Li, N. Ma, L. Zhang, G. Ling and P. Zhang, *Int. J. Pharm.*, 2022, **612**, 121366.

25 B. L. Gadilohar and G. S. Shankarling, *J. Mol. Liq.*, 2017, **227**, 234–261.

26 X. Zhang, C. Li, J. Liang, J. Wang, J. Zhang, X. Chen, F. Wang and R. Li, *ChemCatChem*, 2020, **12**, 1212–1219.

27 H. Ye, S. Sun, J. Chen, W. Zhou, M. Zhang and Z. Yuan, *Environ. Sci. Pollut. Res.*, 2021, **28**, 56003–56031.

28 F. Elhi, M. Gantman, G. Nurk, P. S. Schulz, P. Wasserscheid, A. Aabloo and K. Pöhako-Esko, *Molecules*, 2020, **25**(7), 1691.

29 D. S. Aidhy, B. Liu, Y. Zhang and W. J. Weber, *Comput. Mater. Sci.*, 2015, **99**, 298–305.

30 L. Li, H. Gao, Z. Yi, S. Wang, X. Wu, R. Li and H. Yang, *Colloids Surf., A*, 2022, **644**, 128758.

31 H. Lu, L. Xu, B. Wei, M. Zhang, H. Gao and W. Sun, *Appl. Surf. Sci.*, 2014, **303**, 360–366.

32 P. Cruz, E. Granados, M. Fajardo, I. del Hierro and Y. Pérez, *Appl. Catal., A*, 2019, **587**, 117241.

33 Q. Xu, K. Su, J. Chen, Y. Zhong, Y. Zhao, M. Sun and L. Yu, *Nanoscale*, 2025, **17**, 9588–9598.

34 Y. Feng, Z. Zhang, K. Zhao, S. Lin, H. Li and X. Gao, *J. Colloid Interface Sci.*, 2021, **583**, 499–509.

35 X. Guo, C. Liu, W. Hu, Z. Xu, L. Lu, C. Gao and X. Li, *Colloids Surf., A*, 2024, **685**, 133333.

36 J. Li, Z. Wu, S. Zhang, K. Xu, N. Ma, W. Feng, M. Wu, D. Xu, S. Zhang and J. Shen, *CrystEngComm*, 2022, **24**, 1377–1386.

37 S. Yamamoto, K. Takeuchi, Y. Hamamoto, R. Liu, Y. Shiozawa, T. Koitaya, T. Someya, K. Tashima, H. Fukidome, K. Mukai, S. Yoshimoto, M. Suemitsu, Y. Morikawa, J. Yoshinobu and I. Matsuda, *Phys. Chem. Chem. Phys.*, 2018, **20**, 19532–19538.

38 L. Xue, Y. Du, X. Sun, N. Jiang, J. Qu and J. Zhao, *Mater. Sci. Semicond. Process.*, 2022, **141**, 106447.

39 Z. Yuan, L. Zhang, L. Tan, W. Chen, G. Liao, L. Li and J. Wang, *Appl. Surf. Sci.*, 2024, **649**, 159198.

40 X. Wu, N. Qin, L. Yan, R. Ji, D. Wu, Z. Hou, W. Peng and J. Hou, *Front. Chem.*, 2023, **10**, 1102528.

41 X. Yang, Y. Wang, N. He, W. Wan, F. Zhang, B. Zhai and P. Zhang, *Nanotechnology*, 2020, **31**, 375604.

42 V. Vivier, A. Régis, G. Sagon, J. Nedelec, L. T. Yu and C. Cachet-Vivier, *Electrochim. Acta*, 2001, **46**, 907–914.

43 D. Lin, H. Zhang, X. An, L. Chang, A. Alameen, S. Ding, X. Du and X. Hao, *Phys. Chem. Chem. Phys.*, 2021, **23**, 8500–8507.

44 M. R. d. S. Pelissari, L. Pereira Camargo, F. M. L. Pontes and L. H. Dall'Antonia, *Color. Technol.*, 2023, **139**, 742–757.

45 S. M. Abegunde, K. S. Idowu, O. M. Adejuwon and T. Adeyemi-Adejolu, *Resour. Environ. Sustain.*, 2020, **1**, 100001.

46 L. Li, H. Gao, Z. Yi, S. Wang, X. Wu, R. Li and H. Yang, *Colloids Surf., A*, 2022, **644**, 128758.

47 X. Hu, H. Zhao, Y. Liang and R. Chen, *Appl. Catal., B*, 2019, **258**, 117966.

48 B. A. Prasetyo, I. Prasetyo and T. Ariyanto, *Water, Air, Soil Pollut.*, 2023, **234**, 391.

49 J. Ortiz-Bustos, S. Gómez-Ruiz, J. Mazario, M. E. Domine, I. del Hierro and Y. Pérez, *Catal. Sci. Technol.*, 2020, **10**, 6511–6524.

50 B. Gupta, A. K. Gupta, C. S. Tiwary and P. S. Ghosal, *Environ. Res.*, 2021, **196**, 110390.

51 X. Wen, C. Niu, L. Zhang, C. Liang, H. Guo and G. Zeng, *J. Catal.*, 2018, **358**, 141–154.

52 R. Liu, X. Han, R. Liu and Y. Sun, Highly selective photodegradation of ciprofloxacin by molecularly imprinted Fe3O4/g-C3N4, *Mater. Lett.*, 2022, **325**, 132811.

53 A. V. Baskar, N. Bolan, S. A. Hoang, P. Sooriyakumar, M. Kumar, L. Singh, T. Jasemizad, L. P. Padhye, G. Singh, A. Vinu, B. Sarkar, M. B. Kirkham, J. Rinklebe, S. Wang, H. Wang, R. Balasubramanian and K. H. M. Siddique, *Sci. Total Environ.*, 2022, **822**, 153555.

54 F. Wang, N. Ma, L. Zheng, L. Zhang, Z. Bian and H. Wang, *Chemosphere*, 2022, **307**, 135666.

55 S. K. Ray, D. Dhakal and S. W. Lee, *J. Photochem. Photobiol., A*, 2018, **364**, 686–695.

56 L. Soto-Vázquez, F. Rolón-Delgado, K. Rivera, M. C. Cotto, J. Ducongé, C. Morant, S. Pinilla and F. M. Márquez-Linares, *J. Environ. Manage.*, 2019, **247**, 822–828.



57 M. Manasa, P. R. Chandewar and H. Mahalingam, *Catal. Today*, 2021, **375**, 522–536.

58 E. Turiel, G. Bordin and A. R. Rodríguez, *J. Environ. Monit.*, 2005, **7**, 189–195.

59 H. Pérez del Pulgar, J. Ortiz-Bustos, S. Gómez-Ruiz, I. del Hierro and Y. Pérez, *Environ. Sci.: Water Res. Technol.*, 2024, **10**, 2087–2102.

60 Z. Chen, J. Liang, X. Xu, G. He and H. Chen, *J. Mater. Sci.*, 2020, **55**, 6065–6077.

61 A. Yazdanbakhsh, A. Eslami, M. Massoudinejad and M. Avazpour, *Chem. Eng. J.*, 2020, **380**, 122497.

62 S. K. Ray, D. Dhakal and S. W. Lee, *J. Photochem. Photobiol. A*, 2018, **364**, 686–695.

